npj | materials degradation

Article

Published in partnership with CSCP and USTB

https://doi.org/10.1038/s41529-024-00449-7

Improving the degradation and magnetization performance of FePC amorphous alloys by annealing treatment

Check for updates

Z. G. Qi[1], Q. Chen[1], Z. X. Wang[1], Z. Q. Song[1], K. B. Kim[2], J. Pang[3], X. H. Zhang[1] ✉ & W. M. Wang[1] ✉

The $Fe_{80}P_xC_{20-x}$ ingots and amorphous ribbons ($4.5 \le x \le 6.5$) are arc melted and melt spun respectively. The Rhodamine B degradation performance of as spun and annealed ribbons are investigated with various methods. In present alloys, increasing P content (c_P) can inhibit the precipitation of primary α-Fe and graphite phases, and promote the formation of eutectic α-Fe + Fe_3C + Fe_3P phases in ingots and annealed ribbons. With increasing annealing temperature (T_{an}), the primary α-Fe grain size of the ribbons with c_P = 4.5 at.% increases gradually and that of the ribbons with c_P = 6.5 at.% increases firstly and then decreases. The degradation performance and reusability of the ribbons show a similar T_{an}-dependent behavior, which can be explained by the size effect of the galvanic cells. Meanwhile, the saturation magnetisation B_s and coercivity H_c of the ribbons with c_P = 4.5 and 6.5 at.% increase with increasing T_{an}, showing a near-linear change of the reaction rate constant k against ln (B_s·H_c). This work not only studies the mechanism of improving degradation performance for FePC amorphous alloys by annealing treatment, but also reveals a correlation between degradation performance and magnetization performance of FePC alloys.

The extensive use of synthetic dyes in printing and dying industries has brought serious environmental problems[1–3]. Owing to their high surface active sites induced by disordered atomic packing structure and residual internal stress, Fe-based amorphous alloys ribbons are one of the catalysts which are applied in degrading various printing and dying wastewaters[4–9].

In recent years, some treatments are emerging to improve the degradation capacity of Fe-based amorphous alloys ribbons like ball-milling and dealloying[10–12]. The time required for degrading 50% of acid orange 7 solution by the ball-milling FeSiBNbCu amorphous ribbons is only 1/6 of that by as spun ribbons, while the reusable times of the ball-milling ribbons is 6 times larger than that of as spun ribbons[13]. The dealloying $Fe_{73.5}Si_{13.5}B_9Cu_1Nb_3$ amorphous ribbons with the void channels-like morphology presented a significant improvement of catalytic efficiency and reusability[14]. Although the ball-milling and dealloying ribbons exhibit excellent degradation capability in degrading azo dyes, these two treatments are energy- and time- consuming[15,16].

The energy-efficient and time-saving annealing treatment is applied to improve the degradation capacity of Fe-based amorphous alloys ribbons[17–20]. Chen et al. found that the multiphase $(Fe_{73.5}Si_{13.5}B_9Nb_3Cu_1)_{91.5}Ni_{8.5}$ nanocrystalline ribbons show much better degradation capability in Orange II than their metallic glass counterparts, which ascribes to the galvanic cells between the α-Fe nanocrystals and intermetallics[21]. However, it is also reported that $Fe_{78}Si_9B_{13}$ amorphous ribbons showed better degradation performance for dye solution compared to their crystalline ribbons[22,23]. Besides, the defects are inclined to be activated at a quasi-static loading mode in P-added alloy, which may affects their degradation performance[24]. Fe-P-C systems amorphous alloys also have been reported to have high potential for wastewater remediation as they have good magnetization performance, catalytic efficiency and reusability[25]. Thus, the mechanism of annealing on the degradation performance of amorphous ribbons still needs to be clarified and we choose FePC alloys in this research.

On the other hand, the annealing treatment is an important method to improve the magnetization performance of the amorphous alloys[26–28]. Besides, it is reported that the external magnetic field can remarkably enhance Fenton-like catalytic activity and recyclability of $Fe_{78}Si_9B_{13}$ amorphous ribbons and promote the electrochemical catalytic reactions of FeCoNiPB magnetic catalyst[29,30]. However, almost no research has studied the relationship between magnetization performance and degradation performance of annealed Fe based amorphous.

[1]Key Lab of Liquid Structure and Heredity of Materials, Shandong University, Jinan 250061, China. [2]Department of Nanotechnology and Advanced Materials Engineering, Sejong University, Seoul 05006, Republic of Korea. [3]Qingdao Yunlu Energy Technology Company Limited, Qingdao 266109, China.
✉e-mail: zhangxh@sdu.edu.cn; weiminw@sdu.edu.cn

In this work, we investigated the effects of annealing treatment on the dye degradation performance and magnetization performance of FePC amorphous ribbons. The annealing treatment can promote the precipitation and growth of α-Fe grains in the ribbons. The existence of α-Fe grains with large size facilitates the formation of galvanic cells and promotes inner electron transportation. Thus, annealing the FePC amorphous ribbons at appropriate temperature can improve the degradation performance, B_s (saturation magnetic induction) and H_c (coercivity) of the ribbons significantly, which shows a near-linear relationship between the reaction rate constant k and ln (B_s·H_c).

Results

Characterization of ingots, as spun and annealed ribbons

Figure 1a shows the XRD curves of the $Fe_{80}P_xC_{20-x}$ ingots with x of 4.5, 5, 5.5, 6 and 6.5. With increasing P content (c_P), the phases in the ingots change from α-Fe + Fe_3C phases to α-Fe + Fe_3C + Fe_3P phases. The surface morphologies and corresponding elemental mapping of Fe, P and C of the ingots with x of 4.5, 5.5 and 6.5 are shown in the Fig. 1b–d. The P and C element are mainly present in the ingots as Fe_3P phase and Fe_3C + graphite phases respectively. Meanwhile, with increasing c_P, the content of graphite phase in the ingots decreases gradually, which indicates that increasing c_P can inhibit the precipitation of graphite phase in the ingots.

The XRD analysis of as spun $Fe_{80}P_xC_{20-x}$ (x = 4.5, 5.5 and 6.5) ribbons (labeled as $P4_{as}$, $P5_{as}$ and $P6_{as}$) and the annealed ribbons with c_P = 4.5 and 6.5 at.% are shown in Fig. 2a, c, d. The DSC curves of $P4_{as}$, $P5_{as}$ and $P6_{as}$ with heating and cooling rates of 20 K·min^{-1} are shown in Fig. 2b and the characteristic thermodynamic temperatures are listed in Table 1. Only typical diffuse peaks without any sharp crystalline peaks can be found on the diffraction patterns of $P4_{as}$, $P5_{as}$ and $P6_{as}$, which indicates the amorphous nature of these specimens (Fig. 2a). Meanwhile, $P4_{as}$, $P5_{as}$ and $P6_{as}$ exhibit the similar thermodynamics events upon heating, which can be characterized by three exothermic peaks and two endothermic peaks (Fig. 2b). $P4_{as}$ first forms a primary exothermic peak and then a eutectic exothermic peak, while $P5_{as}$ and $P6_{as}$ first form a eutectic exothermic peak. For studying the primary and eutectic exothermic peaks in the DSC curves, we choose T_{an1} (T_{p1} − 18 K) and T_{an2} (T_{p2} − 13 K) as the annealing temperature (T_{an}) for the ribbons with c_P = 4.5 and 6.5 at.% in the following. Besides, the offset melting temperature (T_l) and solidification temperature (T_s) of $P4_{as}$ are higher than $P5_{as}$ and $P6_{as}$. According to the modern Fe-Graphite alloy phase diagram, this indicates the formation of graphite phase in the melt of $P4_{as}$ during the cooling process, which is consistent with the result of SEM analysis for the ingots (Fig. 1b). Besides, the result of the nano-indentation test is also shown in Supplementary Fig. 1. The hardness (H) and Young's modulus (E) (Supplementary Fig. 1b) can be deduced from the nano-indentation curves (Supplementary Fig. 1a). The H and E of as spun $Fe_{80}P_xC_{20-x}$ (x = 4.5, 5.5 and 6.5) ribbons have an increasing trend with increasing P content (c_P) (Supplementary Fig. 1b). The ratio of hardness to Young's modulus (H/E) can reflect the abrasion resistance of the ribbon: the higher the H/E value, the better the abrasion resistance[31]. With increasing c_P, the abrasion resistance of the ribbons decreases gradually.

Only sharp α-Fe diffraction peaks emerge on the diffuse peaks of the annealed ribbons with c_P = 4.5 at.% (Fig. 2c), which indicates the coexistence of amorphous and α-Fe crystallite structure, and the primary exothermic peak in DSC curves of $P4_{as}$ is mainly composed of primary α-Fe phase. Meanwhile, with increasing T_{an}, the intensity of (200) peak in the annealed ribbons with c_P = 4.5 at.% increases remarkably. Based on Sherrer equation, a higher intensity of (200) peak of α-Fe phase is corresponding to a larger α-Fe grain size[32]. Thus, with increasing T_{an}, the primary α-Fe grain size of the ribbons c_P = 4.5 at.% increases rapidly. Similarly, the ribbon with c_P = 6.5 at.% annealed at T_{an1} is mainly composed of α-Fe diffraction peaks (Fig. 2d). The α-Fe peaks of the annealed ribbon with c_P = 6.5 at.% are normalize and the relative intensity of (200) peak the ribbon with c_P = 6.5 at.% annealed at T_{an1} is higher than that of T_{an2}, which indicates that the α-Fe grain size of the former is larger than that of the latter. Meanwhile, the eutectic α-Fe + Fe_3C + Fe_3P phases emerge on the diffuse peaks of the ribbon with c_P = 6.5 at.% annealed at T_{an2}, which indicates that the eutectic peak in DSC curves of $P6_{as}$ is mainly composed of eutectic α-Fe + Fe_3C + Fe_3P phases. Thus, increasing c_P inhibits the formation of primary α-Fe phase and promotes the formation of eutectic α-Fe + Fe_3C + Fe_3P phases in annealed ribbons. For convenience, the ribbons with c_P = 4.5 at.% annealed at T_{an1} and T_{an2} and the ribbons with c_P = 6.5 at.% annealed at T_{an1} and T_{an2} are labeled as $P4_{an1}$, $P4_{an2}$, $P6_{an1}$ and $P6_{an2}$ respectively in the following.

Figure 3 shows the fracture surface morphology and corresponding elemental mapping of as spun and annealed ribbons after tensile fracture. The typical dimple structure can be observed on the fracture surface of $P4_{as}$ and $P6_{as}$ and the dimple structure disappears gradually with increasing T_{an} (Fig. 3a–f), which indicates that the annealing treatment makes the release of internal stress and the change of atomic structure. The elemental mapping shows that the Fe, P and C element distribute uniformly in $P4_{as}$. With

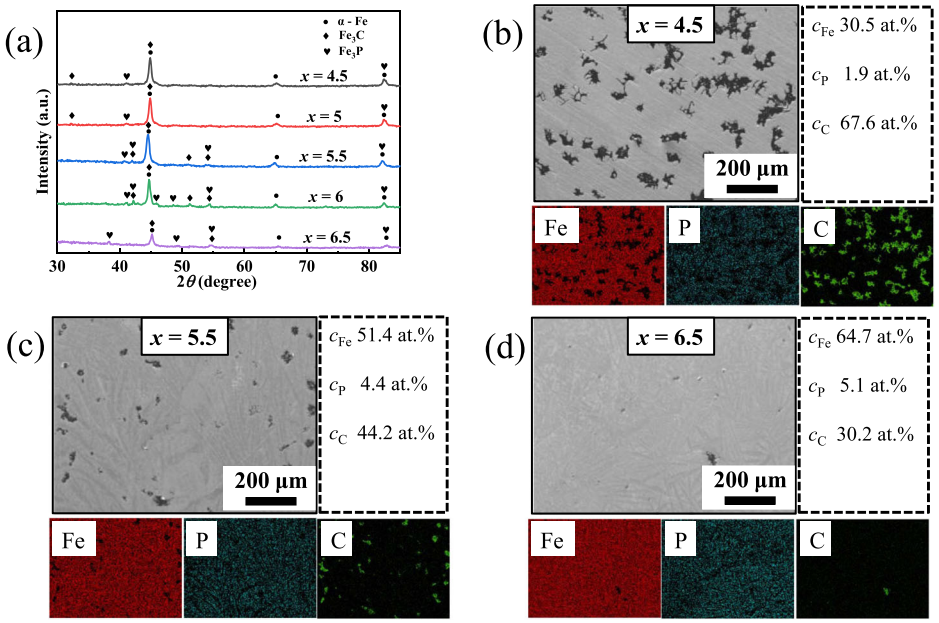

Fig. 1 | The XRD analysis, surface morphologies and corresponding elemental mapping of Fe, P and C of $Fe_{80}P_xC_{20-x}$ ($4.5 \le x \le 6.5$) ingots. a XRD curves of the $Fe_{80}P_xC_{20-x}$ ingots with x of 4.5, 5, 5.5, 6 and 6.5. The microstructure morphologies and corresponding elemental mapping of Fe, P and C of the $Fe_{80}P_xC_{20-x}$ ingots with x = (**b**) 4.5, (**c**) 5.5 and (**d**) 6.5. The dashed box shows the corresponding average composition measured by elemental mapping and the black lines in the figures are the marked scale bars.

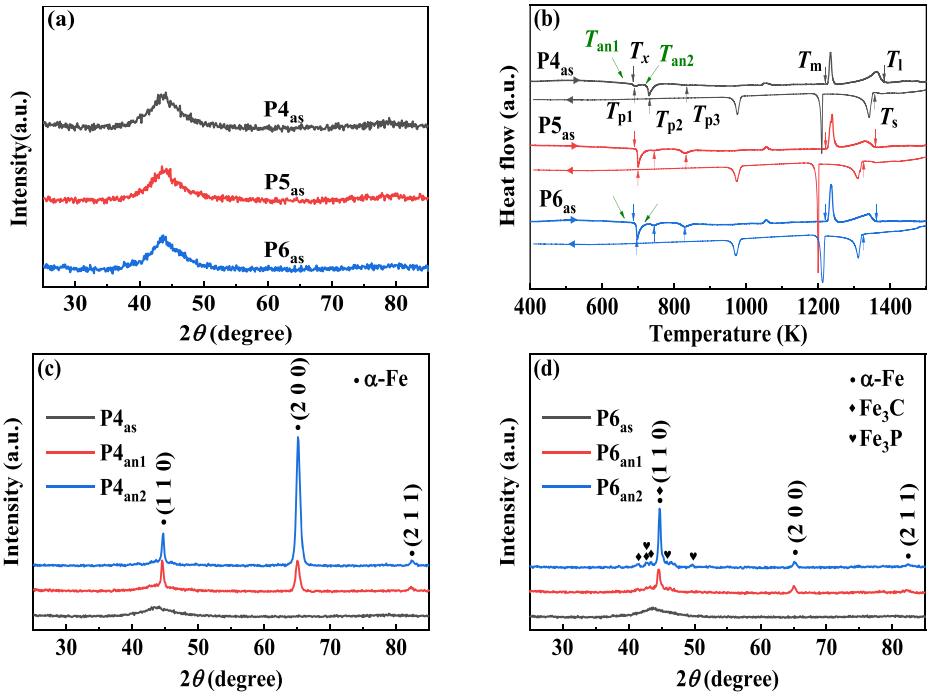

Fig. 2 | The XRD analysis of as spun and annealed $Fe_{80}P_xC_{20-x}$ ($4.5 \le x \le 6.5$) ribbons. a XRD curves of as spun $Fe_{80}P_xC_{20-x}$ (x = 4.5, 5.5 and 6.5) ribbon (denoted as $P4_{as}$, $P5_{as}$ and $P6_{as}$ respectively). **b** DSC curves of $P4_{as}$, $P5_{as}$ and $P6_{as}$ under the heating and cooling rates of 20 K·min^{-1}. XRD curves of as spun and annealed (**c**) $Fe_{80}P_{4.5}C_{15.5}$ ribbons ($P4_{as}$, $P4_{an1}$ and $P4_{an2}$) and (**d**) $Fe_{80}P_{6.5}C_{13.5}$ ribbons ($P6_{as}$, $P6_{an1}$ and $P6_{an2}$).

increasing T_{an}, the C atoms segregate on the surface of the ribbons with c_P = 4.5 at.% gradually (Fig. 3a–c). Combined with the result of EDS analysis for points 1 and 2 (Table 2), the c_C in carbon-rich region reaches to more than 90%, thus we can confirm that C atoms segregate on the surface of $P4_{an1}$ and $P4_{an2}$ as the form of graphite phase. More graphite phase is precipitated on the surface as the ribbons with c_P = 4.5 at.% are annealed at a higher T_{an}. The elemental mapping shows that the Fe and P element distribute uniformly in $P6_{as}$, $P6_{an1}$ and $P6_{an2}$ (Fig. 3d–f). Besides, we perform the EDS analysis for the surface of $P6_{an2}$, the c_{Fe} and c_C in point 3 are much higher and lower than points 1 and 2, which indicates the existence of Fe-C compounds in $P6_{an2}$. Thus, increasing c_P can inhibit the precipitation of graphite phase in the annealed ribbons, which is consistent with the result of SEM analysis for the ingots (Fig. 1) and DSC analysis for the ribbons (Fig. 2b).

RhB degradation performance of as spun and annealed ribbons

Fenton/Fenton-like reactions are highly efficient advanced oxidation processes (AOPs) in wastewater remediation by producing reactive species with a high redox potential to decompose stable and harmful industrial organic effluents into nontoxic and ubiquitous substances. The process of Fenton-like degradation of azo dyes with Fe-based alloys has been revealed to occur in three steps[33]:

$$Fe^0 + H_2O_2 \rightarrow Fe^{2+} + 2OH^- \quad (1)$$

$$Fe^{2+} + H_2O_2 \rightarrow Fe^{3+} + \cdot OH + OH^- \quad (2)$$

$$\cdot OH + \text{organics} \rightarrow \text{products} \quad (3)$$

H_2O_2 react with the zero-valent iron on the surface of the ribbons to produce Fe^{2+} and the as-produced highly reactive hydroxyl ·OH in Eq. (2) is able to oxidize and decompose the organic pollutants from waste water, including Rhodamine B (RhB) solution.

The UV-Vis absorbance spectra of RhB solution after processing with none ribbon, the as spun and annealed ribbons with c_P = 4.5 and 6.5 at.% for a series of time intervals (t_r = 0 ~ 17 min) are presented in Supplementary Fig. 2. The spectra of RhB solution have a major absorption peak at about 554 nm, which is used to quantitatively calculate the concentration of RhB solution[34]. The intensity of this peak of the solution without ribbon remain almost unchanged within 17 mins. In comparison, the intensity of this peak with all ribbons decreases gradually over the whole reaction, corresponding to the reduction of RhB concentration. This illustrates the important role of the catalyst for the degradation of RhB solution. Meanwhile, the normalized concentration (c_t/c_0) of six ribbons for RhB solution is obtained with the peak values at 554 nm and shown in Fig. 4a. c_0 is the initial concentration of RhB solution (mg·L^{-1}), and c_t is the instant RhB solution concentration (mg·L^{-1}) at time t_r. The degradation kinetics are fitted with the pseudo-first-order kinetic model as follows[35]:

$$c_t = c_0 \exp(-kt_r) \quad (4)$$

where k is the reaction rate constant in min^{-1}. Then the degradation reaction rate constant can be derived as follows:

$$k = \ln\left(\frac{C_0}{C_t}\right)/t_r \quad (5)$$

Generally, k and time required for degrading 90% RhB solution ($t_{90\%}$) describe the degradation performance of the ribbons. The lager the k and smaller the $t_{90\%}$, the better the ribbons' degradation performance. According to the ln (c_0/c_t)-t_r curves, the k of as spun and annealed ribbons for RhB solution is 0.21~0.37 min^{-1}, with the fitting goodness $R^2 \ge 0.99$ (Fig. 4b). Meanwhile, the $t_{90\%}$ of as spun and annealed ribbons is 7~11 min. Their k and $t_{90\%}$ are summarized in Fig. 4c, d. The degradation performance of $P6_{as}$ is worse than $P4_{as}$, which ascribes to that Fe-P bonds release less Fe participating in the Fenton-like reaction than Fe-C bonds[5]. Meanwhile, with increasing c_P, the abrasion resistance of as spun ribbons get worse gradually (Supplementary Fig. 1), which is similar to their degradation performance, i.e. the worse the degradation performance of the ribbons. As shown in Fig. 3a, d, the thickness of $P4_{as}$ is higher than that of $P6_{as}$. Due to the different cooling rates of wheel and air sides, the structure heterogeneity of $P4_{as}$ should be higher than $P6_{as}$; meanwhile, the structural heterogeneity is beneficial for the glass's ductility[36], it is expected that $P4_{as}$ has a higher abrasion resistance. The structural heterogeneity can facilitate the formation of galvanic cell and enhance the degradation performance of the ribbons[20].

Table 1 | Thermal properties of as spun $Fe_{80}P_xC_{20-x}$ (x = 4.5, 5.5 and 6.5) ribbon deduced from the DSC curves

Alloy	Onset crystallization temperature T_x (K)	Primary crystallization peak temperature T_{p1} (K)	Secondary crystallization peak temperature T_{p2} (K)	Third crystallization peak temperature T_{p3} (K)	Onset melting temperature T_m (K)	Offset melting temperature T_l (K)	Solidification temperature T_s (K)	First annealing temperature $T_{an1} = T_{p1} - 18$ (K)	Second annealing temperature $T_{an2} = T_{p2} - 13$ (K)
$P4_{as}$	682	691	730	834	1225	1384	1352	673	717
$P5_{as}$	691	701	744	830	1224	1369	1322	-	-
$P6_{as}$	687	698	740	830	1225	1360	1322	680	727

Hence, for the as spun amorphous ribbons, the abrasion resistance may indirectly evaluate the degradation performance. Besides, for c_P = 4.5 at.%, the ribbons have the same $t_{90\%}$ and their k increases gradually with increasing T_{an}. For c_P = 6.5 at.%, the k of the ribbons increases firstly and then decreases with increasing T_{an} and their $t_{90\%}$ is on the contrary. With increasing T_{an}, the degradation performance and reusability of the ribbons with c_P = 4.5 at.% get better gradually and the ribbons with c_P = 6.5 at.% become better firstly and then worse.

The hydrophilicity has a great influence on the catalytic activity of the catalyst, so the contact angle (CA) test of the as spun and annealed ribbons with c_P = 4.5 and 6.5 at.% is performed. With increasing T_{an}, the CA value of the ribbons with c_P = 4.5 at.% decreases gradually (Fig. 4e) and that of the ribbons with c_P = 6.5 at.% decreases firstly and then increases (Fig. 4f), which is correlated with their k values negatively. As we know, the lower the CA value, the higher the ribbon's hydrophilicity. Thus, the CA tests confirms the argument: the higher the hydrophilicity, the better the degradation performance of the ribbons. According to the reference, the existence of ferric deposition on the surface can increase the surface roughness and hydrophilicity of the ribbons[37]. The surface morphologies of as spun and annealed ribbons with c_P = 4.5 and 6.5 at.% before degradation are shown in Supplementary Fig. 4. Apparently, with increasing T_{an}, the Fe oxides appears on the surface of the ribbons with c_P = 4.5 and 6.5 at.% gradually. Meanwhile, with increasing T_{an}, the α-Fe phase and Fe oxides of the ribbons with c_P = 4.5 at.% increase gradually and the α-Fe grain size of the ribbons with c_P = 6.5 at.% increases firstly and then decreases, thus the hydrophilicity of the ribbons after annealing have distinct changes.

Reusability of as spun and annealed ribbons

The reusability of materials are of importance to evaluate the potential of polluted water remediation and the reusability test results of the as spun and annealed ribbons with c_P = 4.5 and 6.5 at.% are shown in Fig. 5. It takes more than 25 min to degrade 90% of RhB solution for $P4_{as}$ and $P4_{an1}$ in cycle 3, while $P4_{an2}$ are capable of degrading 90% of RhB solution within 25 min for 5 cycles. Figure 5a shows the normalized concentration (c_t/c_0) of RhB solution using $P4_{as}$ and $P4_{an1}$ from cycle 1 to cycle 3, and $P4_{an2}$ from cycle 1 to cycle 5. With increasing cycle from 1 to 3 for $P4_{as}$ and $P4_{an1}$, the k value decreases and $t_{90\%}$ value increases gradually, and the k and $t_{90\%}$ values reach to about 0.1 min^{-1} and 29 min in cycle 3 (Fig. 5b). Meanwhile, with increasing cycle from 1 to 5 for $P4_{an2}$, the k value decreases at first and stabilizes at about 0.15 min^{-1} in the end, and the $t_{90\%}$ value increases at first and stabilizes at 19 min in the end. Apparently, with increasing T_{an}, the reusability of the ribbons with c_P = 4.5 at.% gets better gradually.

In comparison, it takes more than 25 min to degrade 90% of RhB solution for $P6_{as}$ in cycle 3, while $P6_{an1}$ and $P6_{an2}$ are capable of degrading 90% of RhB solution within 25 min for 5 cycles. Figure 5c shows the normalized concentration (c_t/c_0) of the RhB solution using $P6_{as}$ from cycle 1 to cycle 3, and $P6_{an1}$ and $P6_{an2}$ from cycle 1 to cycle 5. The k and $t_{90\%}$ values of $P6_{as}$ remain almost stable with increasing cycle from 1 to 2, and the k value decreases and $t_{90\%}$ value increases sharply in cycle 3 (Fig. 5d). Meanwhile, the $t_{90\%}$ values of $P6_{an1}$ and $P6_{an2}$ are around 13 and 23 min, and their k values stabilize at about 0.25 and 0.1 min^{-1} at the end of the cycle test, respectively. Apparently, $P6_{an1}$ has higher k value and lower $t_{90\%}$ value than $P6_{an2}$ during the cycle test, which is different with $P4_{an1}$ and $P4_{an2}$. Thus, with increasing T_{an}, the reusability of the ribbons with c_P = 6.5 at.% gets better firstly and then worse. Meanwhile, increasing c_P can improve the reusability of as spun and annealed ribbons appropriately.

Magnetization performance of as spun and annealed ribbons

According to the reference, the external magnetic field can improve the degradation performance of the ribbons, thus we believe that there is a relationship between the degradation performance for RhB solution and magnetization performance of the ribbons[29]. The permeability (μ) of all ribbons is measured in the frequency range of 1–1000 kHz at 20 $A{\cdot}m^{-1}$ applied field and the results are shown in the Supplementary Fig. 5a. With the precipitation of the crystalline phase in the ribbons, the μ decreases

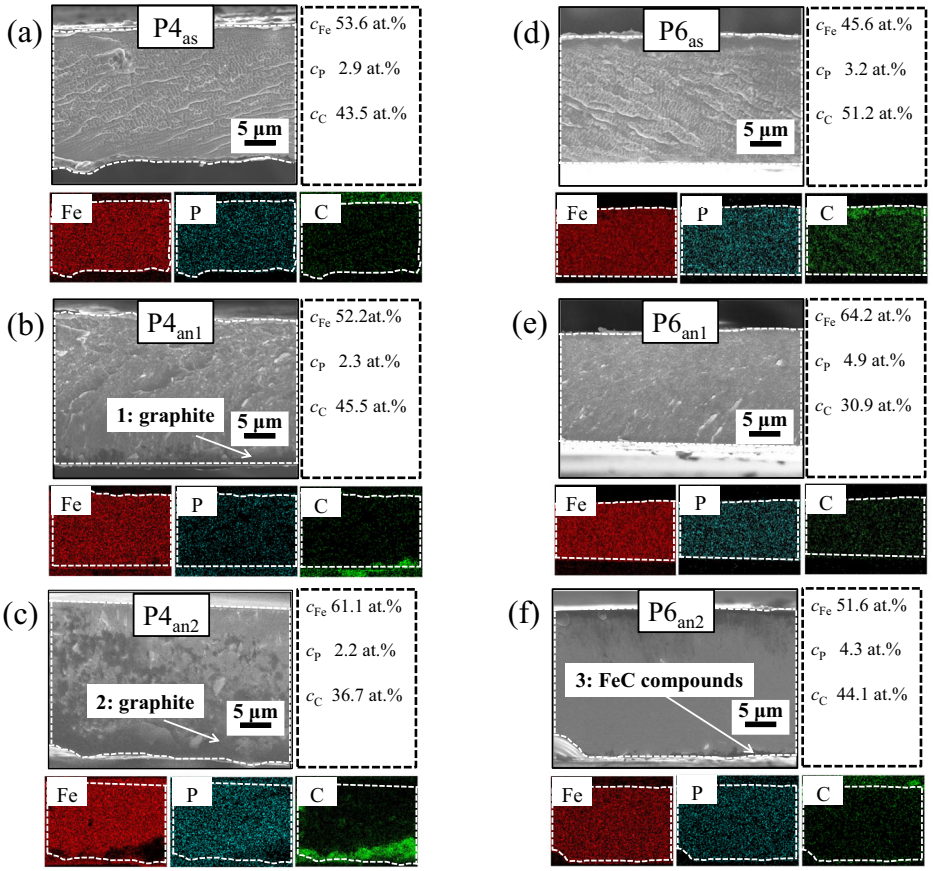

Fig. 3 | The fracture surface morphologies and corresponding elemental mapping of Fe, P and C of as spun and annealed $Fe_{80}P_xC_{20-x}$ ($x = 4.5$ and 6.5) ribbons. a $P4_{as}$, (**b**) $P4_{an1}$, (**c**) $P4_{an2}$, (**d**) $P6_{as}$, (**e**) $P6_{an1}$ and (**f**) $P6_{an2}$. The dashed box shows the corresponding average composition measured by elemental mapping and the black lines in the figures are the marked scale bars.

rapidly with increasing T_{an}, which confirms that the amorphous structure can improve the μ of the ribbons[38].

The *B-H* hysteresis loops of the as spun and annealed ribbons with $c_P = 4.5$ and 6.5 at.% measured by the VSM are shown in Fig. 6a. The B_s (saturation magnetisation) of the ribbons are obtained according to the enlarged part of the VSM *B-H* hysteresis loops (inset of Fig. 6a) and listed in Table 3. For as spun ribbons, the B_s of $P4_{as}$ is greater than $P6_{as}$, which ascribes to the different electron configurations of P and C atoms[39]. With increasing T_{an}, the B_s of the ribbons with $c_P = 4.5$ and 6.5 at.% increases gradually, which ascribes to the precipitation of α-Fe phase in the ribbons.

The H_c (coercivity) of amorphous soft magnetic material $P4_{as}$ and $P6_{as}$ are obtained according to the *B-H* hysteresis loops, which is measured by DC *B-H* loop tracer (Fig. 6b). Apparently, the H_c of $P6_{as}$ is smaller than $P4_{as}$, which indicates that the addition of appropriate P element can improve the soft magnetization performance of the FePC amorphous alloys. The DC *B-H* loop tracer is not accurate for the hard or semi-hard magnetic material annealed ribbons, which ascribes to that the maximum magnetic field applied by DC *B-H* loop tracer does not make the materials reach saturation and this will have a great impact on the measurement of H_c of the materials. Supplementary Fig. 5b shows the *B-H* hysteresis loops of $P4_{an1}$ under different magnetic field range measured by DC *B-H* loop tracer. With increasing magnetic field from 1000 to 20,000 $A{\cdot}m^{-1}$ applied by DC *B-H* loop tracer, the measurement result of H_c of $P4_{an1}$ increases from 258 to 3804 $A{\cdot}m^{-1}$ gradually. Thus, the H_c (Oe) of annealed ribbons are obtained according to the enlarged part of the VSM *B-H* hysteresis loops (Fig. 6c) and are listed in Table 3.

For $c_P = 4.5$ at.%, the H_c of the ribbons increases gradually with increasing T_{an}, which ascribes to that the α-Fe phase formed by annealing treatment induces the magnetocrystalline anisotropy. And as the quasi dislocation dipole, it makes the domain wall movement of pinning site pile increase[40]. In comparison, for $c_P = 6.5$ at.%, the H_c of ribbons also increases gradually with increasing T_{an}, which is determined by the precipitation of eutectic α-Fe + Fe_3C + Fe_3P phases.

Figure 6d shows the k vs. ln ($B_s{\cdot}H_c$) for all ribbons and we performed a linear fit for these points. Surprisingly, these points have a near-linear relationship and the fitting goodness R^2 reaches to 0.9030. According to the previous research[41], the additional magnetic field can generate the gradient magnetic force on the surface, which can accelerate Fe^{3+}/Fe^{2+} cycle for Fenton like reaction. The Fenton-like reaction of the ribbons takes place under the magnetic stirring, so the ribbons are affected by the additional magnetic field. With increasing B_s, the gradient magnetic force increases, which can improve the degradation performance of the ribbons finally. Besides, the H_c represents the ability of the material to resist demagnetization after magnetization[42]. Thus, with increasing H_c, the demagnetization resistance of the ribbons increases and the ribbons are more affected easily by additional magnetic field continually, which can also improve the degradation performance of the ribbons.

For strengthen the near-linear relationship for k vs. ln ($B_s{\cdot}H_c$), the ribbon with $c_P = 6.5$ at.% is annealed at T_{an3} ($T_{p1} - 68$ K) ($P6_{an3}$) and T_{an4} ($T_{p1} - 28$ K) ($P6_{an4}$) complementally. The corresponding data of XRD analysis, magnetization performance and degradation performance is shown in Supplementary Fig. 6 and Supplementary Table 1. These points still have a near-linear relationship and the fitting goodness R^2 reaches to 0.8959 (Fig. 7).

Table 2 | General composition of 1-3 points measured by EDS in Fig. 3 b, c, f

Alloy	EDS Point	c_{Fe} (at.%)	c_P (at.%)	c_C (at.%)
$P4_{an1}$	1	7.6	0.6	91.8
$P4_{an2}$	2	6.0	0.3	93.7
$P6_{an2}$	3	54.7	4.6	40.7

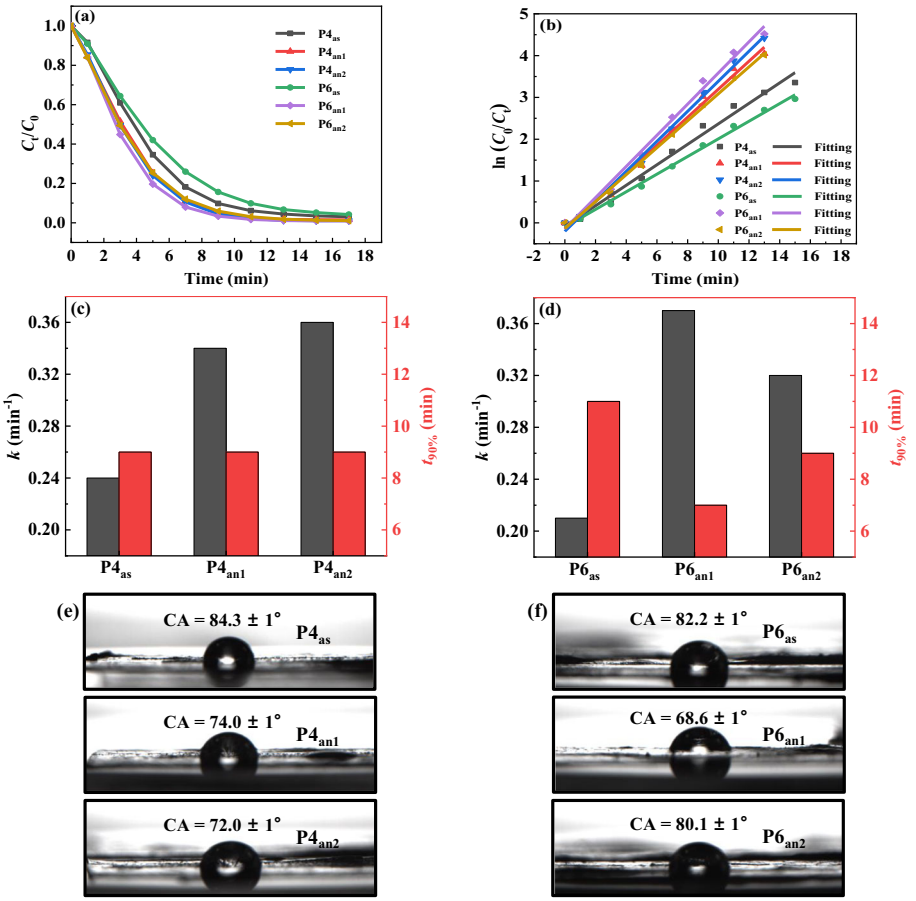

Fig. 4 | The RhB degradation performance and contact angles (CA) of as spun and annealed $Fe_{80}P_xC_{20-x}$ ($x = 4.5$ and 6.5) ribbons. a The normalized concentration change of RhB solution using as spun and annealed $Fe_{80}P_xC_{20-x}$ ($x = 4.5$ and 6.5) ribbons ($P4_{as}$, $P4_{an1}$, $P4_{an2}$, $P6_{as}$, $P6_{an1}$ and $P6_{an2}$) during the degradation process. **b** The ln (c_0/c_t)-t_r curves for all ribbons. **c** The reaction rate constant (k) and the time required for degrading 90% RhB solution ($t_{90\%}$) of $P4_{as}$, $P4_{an1}$ and $P4_{an2}$. **d** The k and $t_{90\%}$ of $P6_{as}$, $P6_{an1}$ and $P6_{an2}$.The CA of (**e**) $P4_{as}$, $P4_{an1}$, $P4_{an2}$ and (**f**) $P6_{as}$, $P6_{an1}$, $P6_{an2}$ with RhB solution droplet.

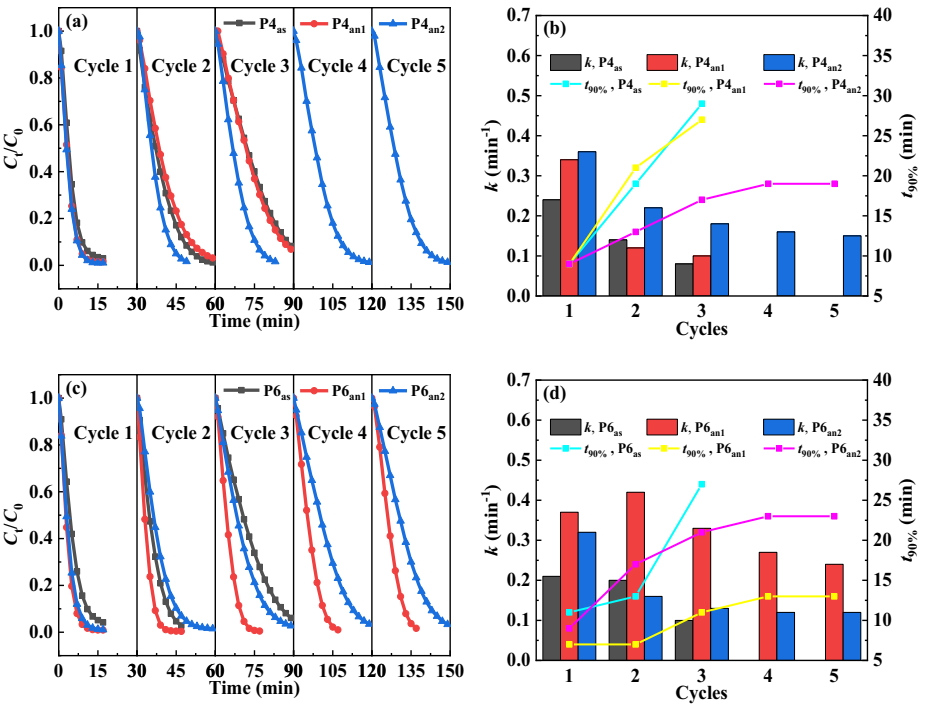

Fig. 5 | The reusability of as spun and annealed $Fe_{80}P_xC_{20-x}$ ($x = 4.5$ and 6.5) ribbons for RhB solution. a The normalized concentration change of RhB solution during the degradation process of as spun and annealed $Fe_{80}P_{4.5}C_{15.5}$ ribbons $P4_{as}$ and $P4_{an1}$ from cycle 1 to cycle 3, and $P4_{an2}$ from cycle 1 to cycle 5. **b** The reaction rate constant k and the time required for degrading 90% RhB solution $t_{90\%}$ vs. reaction cycles for $P4_{as}$, $P4_{an1}$ and $P4_{an2}$. **c** The normalized concentration change of RhB solution during the degradation process of as spun and annealed $Fe_{80}P_{6.5}C_{13.5}$ ribbons $P6_{as}$ from cycle 1 to cycle 3, and $P6_{an1}$ and $P6_{an2}$ from cycle 1 to cycle 5. **d** The reaction rate constant k and the time required for degrading 90% RhB solution $t_{90\%}$ vs. reaction cycles for $P6_{as}$, $P6_{an1}$ and $P6_{an2}$.

Discussion

As the degradation process is surface mediated, it is significant to understand the surface morphology and element changes of the ribbons during the Fenton-like reaction. SEM analysis on the surfaces of the ribbons with $c_P = 6.5$ at.% after degradation together with the electrochemical impedance spectra (EIS) curves are shown in Fig. 8. Before degradation, $P6_{as}$, $P6_{an1}$ and $P6_{an2}$ have a typical smooth surface (Supplementary Fig. 4a–c). After degradation, some angular structure appears on the surface of $P6_{as}$ (Fig. 8a),

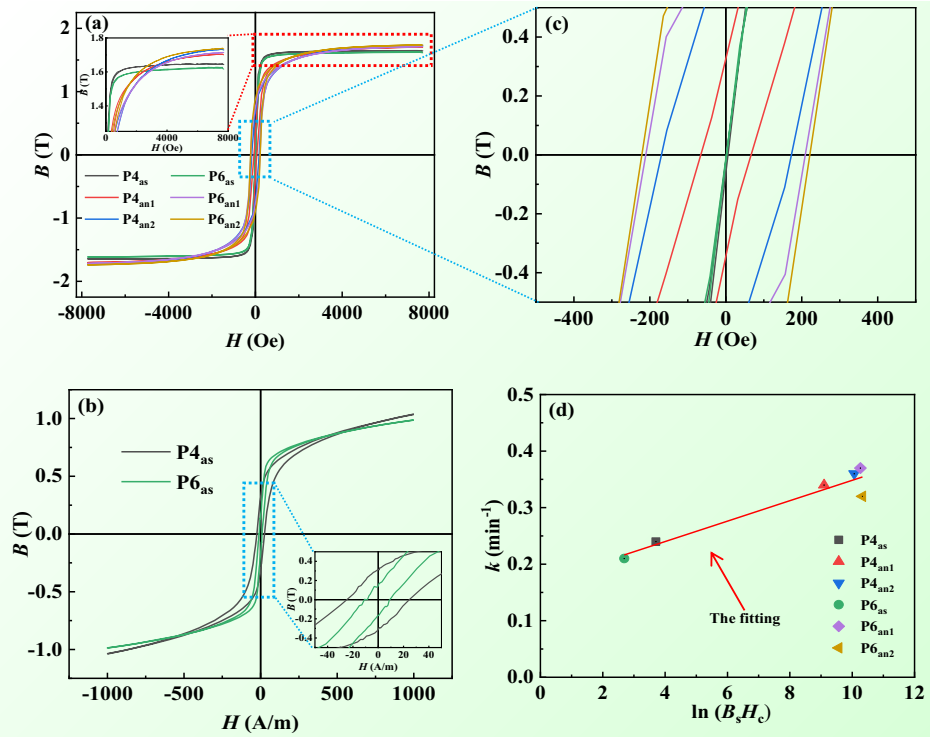

Fig. 6 | The magnetization performance of as spun and annealed $Fe_{80}P_xC_{20-x}$ ($x = 4.5$ and 6.5) ribbons. a *B-H* hysteresis loops of as spun and annealed $Fe_{80}P_{4.5}C_{15.5}$ ribbons ($P4_{as}$, $P4_{an1}$ and $P4_{an2}$) and $Fe_{80}P_{6.5}C_{13.5}$ ribbons ($P6_{as}$, $P6_{an1}$ and $P6_{an2}$) measured by the vibrating sample magnetometer (VSM), the inset in (**a**): the enlarged part of the red border in hysteresis loops. **b** *B-H* hysteresis loops of $P4_{as}$ and $P6_{as}$ measured by DC B-H loop tracer, the inset in (**b**): the enlarged part of the blue border in hysteresis loops. **c** The enlarged part of the blue border in hysteresis loops (**a**). **d** The reaction rate constant k vs. ln (B_s·H_c) for all ribbons.

in comparison, the surface of $P6_{an1}$ has a honeycomb structure (Fig. 8b), which can provide channels for the transfer of Fe atoms and improve the degradation performance and reusability of the ribbons[43]. Some acicular structure replaces the honeycomb structure on the surface of $P6_{an2}$ after degradation, which makes the honeycomb structure in the ribbons decrease and provides less channels for the transfer of Fe atoms (Fig. 8c).

The EDS results on the surface of the ribbons with $c_P = 6.5$ at.% before and after degradation are summarized in Table 4. Apparently, the c_{Fe} on the surface of $P6_{an1}$ and $P6_{an2}$ is higher than $P6_{as}$, which is consistent with the result of EDS analysis for fracture surface (Fig. 3d–f) and explains the better degradation performance and reusability of annealed ribbons. Meanwhile, the c_{Fe} on the surface of these ribbons decreases after degradation, indicating that Fe element plays an important role in the degradation process. There is more O element on the surface of $P6_{as}$ than annealed ribbons after degradation, which indicates that the angular structure is oxide (Fig. 8a). The oxide blocks the release of the internal Fe, which explains the worse degradation performance and reusability of $P6_{as}$. Besides, the fitting results on the EIS data of the ribbons with $c_P = 6.5$ at.% in RhB solution (Fig. 8d) are listed in Supplementary Table 2. With increasing T_{an}, the resistance of transfer charge (R_t) of the ribbons decreases firstly and then increases, which indicates the corrosion rate increases firstly and then decreases. The maximum corrosion rate of $P6_{an1}$ corresponds to its best degradation performance, which explains the formation of honeycomb structure during the degradation process.

Table 3 | The reaction rate constant *k*, saturation magnetization B_s, coercivity H_c and ln (B_s·H_c) of as spun and annealed $Fe_{80}P_{4.5}C_{15.5}$ ribbons and $Fe_{80}P_{6.5}C_{13.5}$ ribbons

Alloy	Reaction rate constant k (min^{-1})	Saturation magnetization B_s (T)	Coercivity H_c (Oe)	Coercivity H_c ($A{\cdot}m^{-1}$)	ln (B_s·H_c) ($T{\cdot}A{\cdot}m^{-1}$)
$P4_{as}$	0.24	1.64	-	24.80	3.71
$P4_{an1}$	0.34	1.70	66.15	5263.65	9.10
$P4_{an2}$	0.36	1.73	171.14	13618.49	10.07
$P6_{as}$	0.21	1.62	-	9.10	2.69
$P6_{an1}$	0.37	1.71	210.47	16748.27	10.26
$P6_{an2}$	0.32	1.74	221.18	17600.95	10.33

The XPS analysis on the surface of the ribbons with $c_P = 6.5$ at.% before and after degradation like the Fe $2p_{3/2}$, P 2p, C 1 s and O 1 s spectra are shown in Fig. 9 and Supplementary Fig. 7. The XPS parameters are listed in Supplementary Table 3. The Fe $2p_{3/2}$ spectrum of the ribbons with $c_P = 6.5$ at.% can be divided into Fe^0 (707.0 eV), Fe^{2+} (710.5 eV) and Fe^{3+} (711.2 eV) according to the ref. 44 Before degradation, with increasing T_{an}, the Fe^0 peak area fraction (f_{Fe0}) of the ribbons decreases gradually, indicating the involvement of Fe^0 oxidation during the annealing process (Fig. 9a). Meanwhile, $P6_{an1}$ has the largest sum of $f_{Fe0} + f_{Fe2+}$, which corresponds to its best degradation performance. After degradation, the Fe^0 peak disappears and f_{Fe2+} of the ribbons decreases, indicating the involvement of Fe^0 and Fe^{2+} oxidation during the degradation process (Fig. 9b).

The P 2p spectrum of the ribbons with $c_P = 6.5$ at.% consists of P^0 (129.5 and 130.4 eV) and P^{5+} (132.9 eV) peaks[45]. Besides, with increasing T_{an}, the f_{P0} of the ribbons decreases and f_{P5+} increases gradually, indicating that P^0 is oxidized to P^{5+} during the annealing process (Fig. 9c). After degradation, the P^0 peak disappears and the P 2p spectra of the ribbons only consist of P^{5+} peak, indicating that the involvement of P^0 oxidation during the degradation process (Fig. 9d). With increasing T_{an}, the increment of P peak area (ΔA_{sum}) of the ribbons after degradation increases firstly and then decreases. Meanwhile, $P6_{an1}$ has the largest P^{5+} peak area (A_{P5+}) after degradation. According to the ref. 46 the P element has positive effect on accelerating Fe^{3+}/Fe^{2+} cycle and improving the Fenton like reaction rate. Thus, the reusability of the ribbons with $c_P = 6.5$ at.% is better than that of the ribbons with $c_P = 4.5$ at.%, and the reusability of the ribbons with $c_P = 6.5$ at.% become better firstly and then worse with increasing T_{an}.

The C 1 s spectrum of the ribbons with $c_P = 6.5$ at.% consists of three peaks at C^0 (284.8 eV), '–C–O–' (286.4 eV) and '–C = O–' (288.5 eV) according to the ref. 47 The annealing treatment has little effect on the ribbons before degradation (Supplementary Fig. 7a). The f_{-C-O-} and $f_{-C=O-}$ of the ribbons increases after degradation, indicating that the oxidation of C is accompanied during the degradation (Supplementary Fig. 7b).

The O 1 s spectrum of the ribbons with $c_P = 6.5$ at.% consists of two peaks at 'Fe–O' (530.0 eV), 'P/C–O' (531.6 eV)[48]. Before degradation, with increasing T_{an}, the f_{Fe-O} of the ribbons decreases and $f_{P/C-O}$ increases gradually (Supplementary Fig. 7c), which is consistent with the result of P 2p and C 1 s spectra. The f_{Fe-O} of the ribbons decreases after degradation, which confirms the involvement of Fe element during the degradation process (Supplementary Fig. 7d). Besides, $P6_{an1}$ and $P6_{an2}$ have the highest and lowest $f_{P/C-O}$ after degradation, respectively, which explains the higher k and lower $t_{90\%}$ of $P6_{an1}$ compared with $P6_{an2}$ during the cycle test and is consistent with the result of P 2p spectra (Fig. 9d). $P6_{as}$ also has a higher $f_{P/C-O}$ than $P6_{an2}$ after degradation, which explains its higher k and lower $t_{90\%}$ in cycle 2 (Fig. 5d).

The P element has positive effect on the degradation performance and reusability of the ribbons in the above analysis[46]. However, the degradation performance and reusability of $P6_{an2}$ is worse than $P4_{an2}$ and P_{6an1}, but P_{6an2} has a higher nominent c_P than P_{4an2} and there is more P element on the surface of $P6_{an2}$ than $P6_{an1}$ before degradation (Fig. 9c). Thus, we believe that the degradation performance of the ribbons is also related to their microstructure.

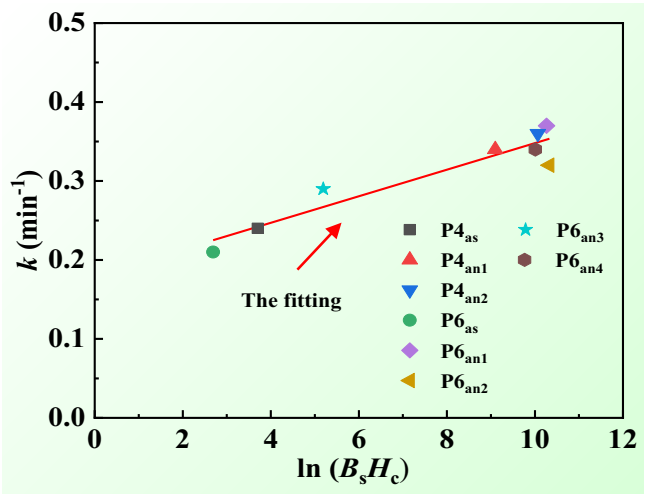

Fig. 7 | The reaction rate constant k vs. ln (B_s·H_c) for annealed $Fe_{80}P_{6.5}C_{13.5}$ ribbons ($P6_{an3}$ and $P6_{an4}$) and other ribbons.

To unveil the microstructure of the alloys, TEM analysis is performed on the as spun and annealed ribbons with $c_P = 6.5$ at.% and shown in Figs. 10 and 11. No crystallite is observed in TEM bright-filed images of $P6_{as}$ and the corresponding FFT patterns consist only of a typical diffraction halo, which indicates the homogeneous amorphous structure of $P6_{as}$ (Fig. 10a–c). The TEM bright-filed images and corresponding FFT patterns of $P6_{an1}$ reveal the existence of α-Fe crystallite, which has a grain size of ≈ 500 nm (Fig. 10d–f), and $P6_{an1}$ mainly consists of amorphous matrix and α-Fe grains with large size (Fig. 10g–i). According to the ref. 49 the existence of multiphase crystallite facilitate the formation of galvanic cells, and the grain growth can greatly weaken electron trapping and promote inner electron transportation. The T_{an1} annealing treatment mainly results in the growth of α-Fe grains in $P6_{an1}$. The galvanic effect between α-Fe crystallite and amorphous matrix, and the α-Fe grains with large size can promote inner electron transportation, which can improve the degradation performance and reusability of the ribbons.

Apparently, compared with $P6_{an1}$, the grain size of $P6_{an2}$ is about 50 nm, which is much less than $P6_{an1}$ (Fig. 11a, b). This explains that the degradation performance and reusability of $P6_{an2}$ is worse than $P6_{an1}$. Meanwhile, the T_{an2} annealing treatment promotes the precipitation α-Fe + Fe_3C + Fe_3P eutectic phases in $P6_{an2}$ (Fig. 11c–i), which makes the α-Fe grains size of $P6_{an2}$ smaller than $P6_{an1}$. Thus, the T_{an2} annealing treatment mainly causes the eutectic crystallization in $P6_{an2}$ rather than primary α-Fe crystallization, which is consistent with the XRD and DSC analysis for the ribbons (Fig. 2b, d). The galvanic cell effect generated by multiphase crystallite can promote inner electron transportation effectively[49], which makes the degradation performance and reusability of $P6_{an2}$ better than $P6_{as}$.

With increasing T_{an}, the primary α-Fe grains size of the ribbons with $c_P = 4.5$ at.% increases (Fig. 2c) and their C atom segregation degree rises gradually (Fig. 3a–c), indicating that the segregation of C atoms can promote the precipitation and growth of primary α-Fe grains. The existence of α-Fe crystallite and graphite phase facilitate the formation of galvanic cells, and the primary α-Fe grains growth can promote inner electron transportation[49]. Thus, the degradation performance and

Fig. 8 | Surface morphologies and electrochemical performance of as spun and annealed $Fe_{80}P_{6.5}C_{13.5}$ ribbons after degradation. a $P6_{as}$, (**b**) $P6_{an1}$ and (**c**) $P6_{an2}$; the inset in (**a**–**c**): the enlarged part of (**a**–**c**) and the lines in the figure are the marked scale bars. **d** Nyquist curves and relative fitting results of $P6_{as}$, $P6_{an1}$ and $P6_{an2}$ by equivalent circuit R(C(R(OR))).

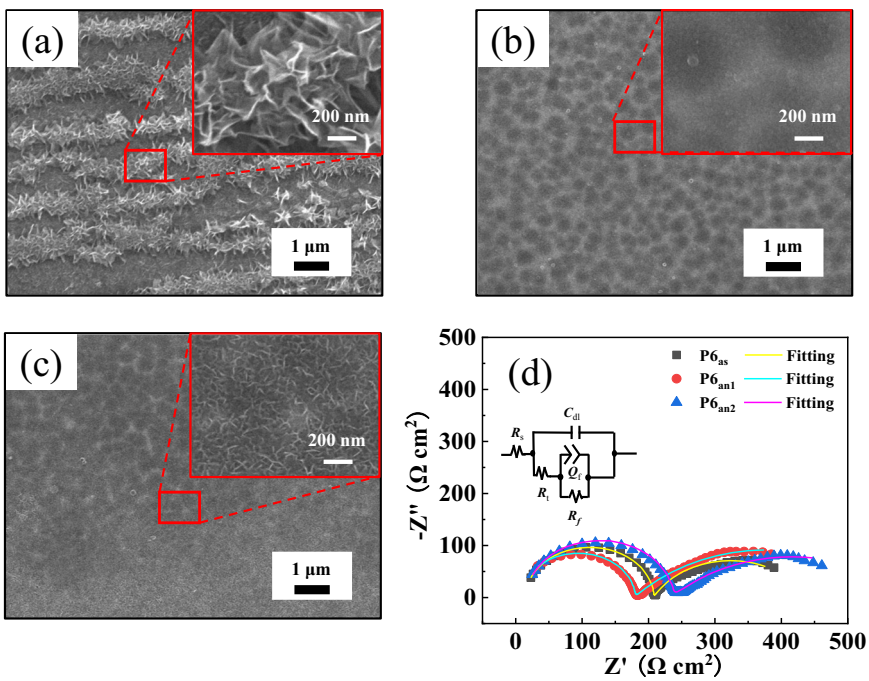

Table 4 | Compositions of the ribbons before (B.D.) and after degradation (A.D.) of as spun and annealed $Fe_{80}P_{6.5}C_{13.5}$ ribbons by EDS analysis

Alloy	B.D.				A.D.			
	c_{Fe} (at.%)	c_P (at.%)	c_C (at.%)	c_O (at.%)	c_{Fe} (at.%)	c_P (at.%)	c_C (at.%)	c_O (at.%)
$P6_{as}$	63.0	5.0	30.6	1.4	27.2	6.8	31.6	34.3
$P6_{an1}$	71.7	6.1	20.6	1.6	43.7	6.3	30.3	19.7
$P6_{an2}$	71.6	6.1	21.0	1.3	40.3	7.0	32.0	20.7

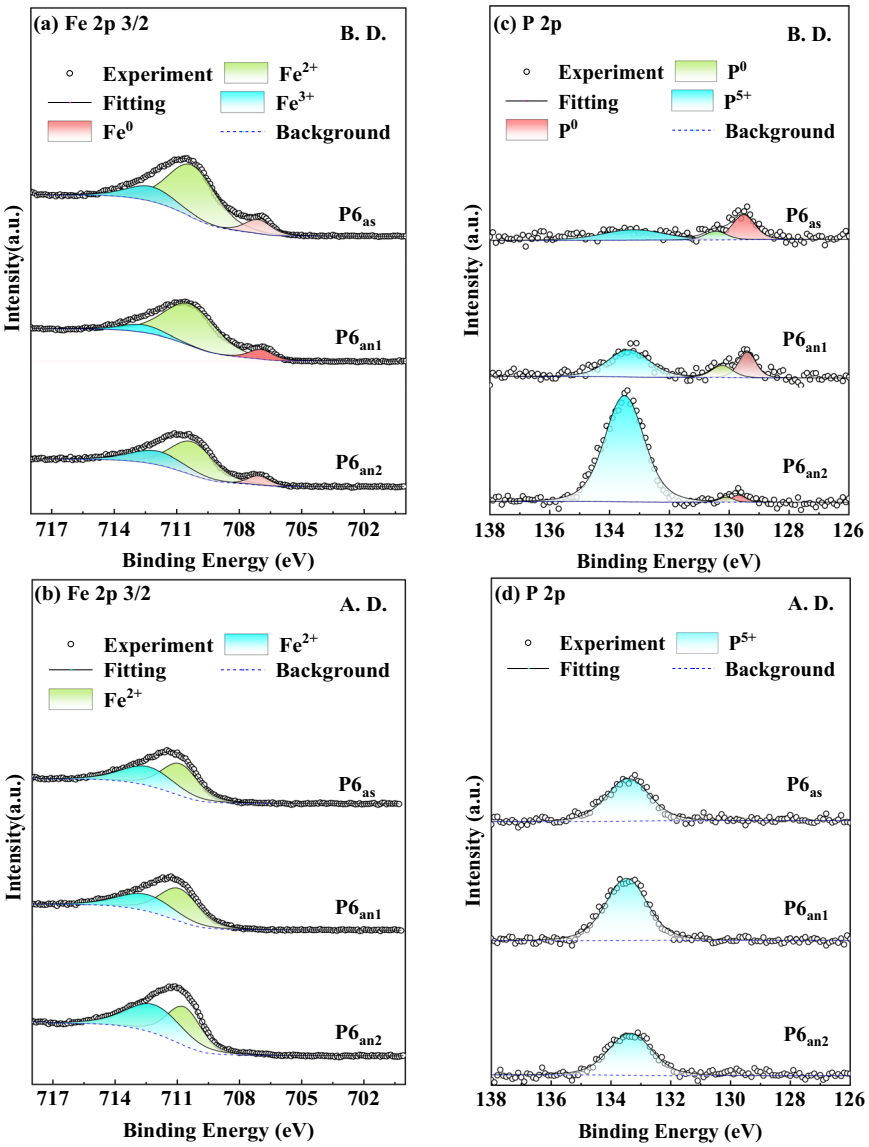

Fig. 9 | XPS spectra in binding energy regions for as spun and annealed $Fe_{80}P_{6.5}C_{13.5}$ ribbons ($P6_{as}$, $P6_{an1}$ and $P6_{an2}$) before degradation (B.D.) and after degradation (A.D.). **a** Fe $2p_{3/2}$ B.D., (**b**) Fe $2p_{3/2}$ A.D., (**c**) P 2p B.D. and (**d**) P 2p A.D.

reusability of the ribbons with $c_P = 4.5$ at.% gets better gradually with increasing T_{an}. This also confirms the discussion of TEM analysis for the ribbons with $c_P = 6.5$ at.%.

The annealing, ball-milling and dealloying are common processing treatments to improve the degradation performance of the amorphous ribbons[35]. Thus, we set $(k_{AP} - k_{AS})/k_{AS}$·100% as the influence rate of one processing method, here AP (after processing) denotes the sample after commending treatment, AS denotes as spun/prepared sample. We compare present $P4_{an2}$ and $P6_{an1}$ with other referenced materials, which are processed by corresponding amorphous alloys with annealing (Table 5), ball-milling (Table 6), dealloying (Table 7) and are shown in Fig. 12. Here, $P4_{an2}$ and $P6_{an1}$ have the higher k_{AP} and influence rate for RhB solution than most of the referenced ribbons.

Figure 13 shows the schematic illustration of the pathway of RhB solution degradation for as spun and annealed $Fe_{80}P_xC_{20-x}$ ($x = 4.5$ and 6.5) ribbons ($P4_{as}$, $P4_{an1}$, $P6_{as}$ and $P6_{an1}$). Increasing c_P can accelerate Fe^{3+}/Fe^{2+} cycle in the ribbons for Fenton like reaction. Meanwhile, the annealing treatment can promote the precipitation and growth of α-Fe grains in the ribbons. The existence of α-Fe grains with large size facilitates the formation of galvanic cells and promotes inner electron transportation[49]. Thus, the annealed ribbon with $c_P = 6.5$ at.% have better degradation performance and reusability than the others. Meanwhile, the B_s and H_c of the ribbons with

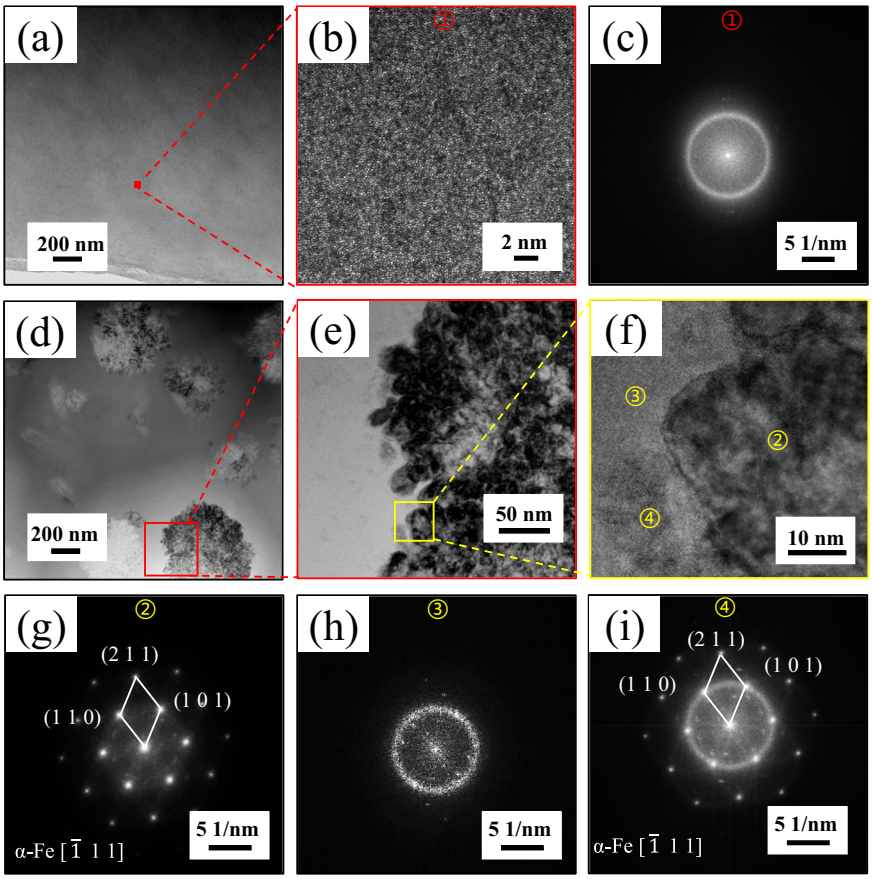

Fig. 10 | The TEM analysis of as spun and annealed $Fe_{80}P_{6.5}C_{13.5}$ ribbons at T_{an1} ($P6_{as}$ and $P6_{an1}$). **a** LRTEM image of $P6_{as}$. **b** HRTEM image of $P6_{as}$ and (**c**) corresponding FFT pattern. **d** LRTEM image of $P6_{an1}$. **e** The enlarged part of the LRTEM image (**d**). **f** HRTEM image of $P6_{an1}$ for yellow border in (**e**), and (**g**–**i**) corresponding FFT pattern. The black lines in the figures are the marked scale bars.

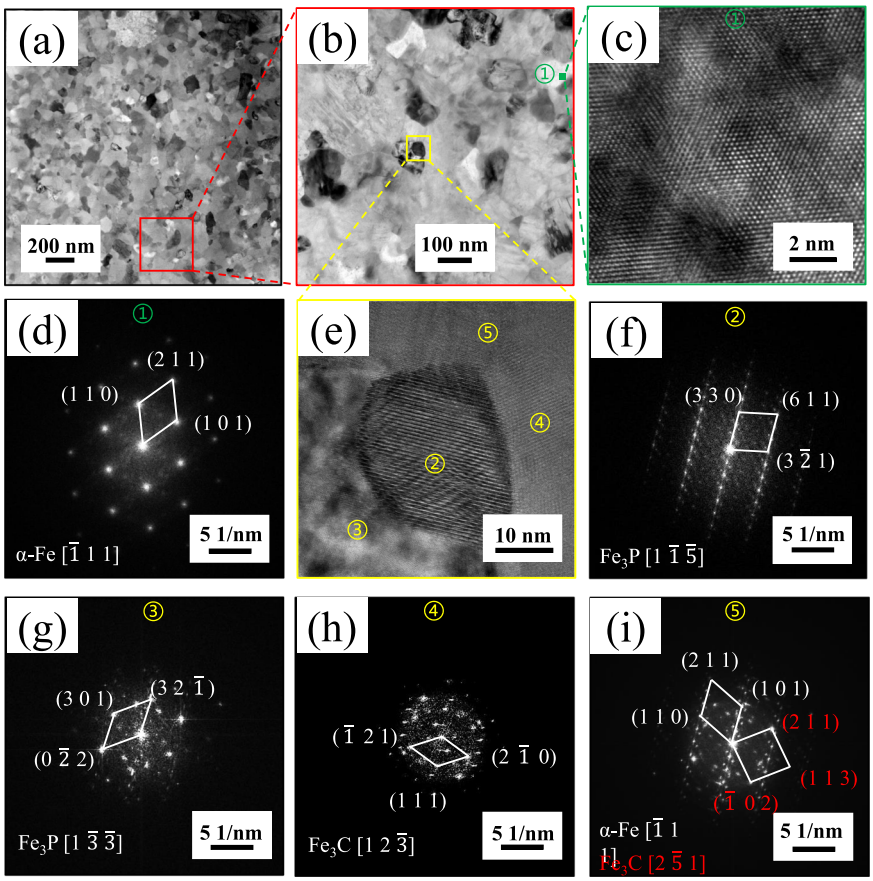

Fig. 11 | The TEM analysis of annealed $Fe_{80}P_{6.5}C_{13.5}$ ribbon at T_{an2} ($P6_{an2}$). **a** LRTEM image of $P6_{an2}$. **b** The enlarged part of the LRTEM image (**a**). **c** HRTEM image of $P6_{an2}$ for ① in (**b**), and (**d**) corresponding FFT pattern. **e** HRTEM image of $P6_{an2}$ for yellow border in (**b**), and (**f**–**i**) corresponding FFT pattern. The black lines in the figures are the marked scale bars.

Table 5 | Current development of wastewater treatment using as spun and annealed ribbons under different conditions

Catalysts	Organic pollutants	c_{Dye} (mg·L^{-1})	$c_{catalysts}$ (g·L^{-1})	c_{H2O2} (mM)	pH	Reaction rate constant of as spun ribbon k_{AS} (min^{-1})	Reaction rate constant of after-processing ribbon k_{AP} (min^{-1})
$Fe_{80}P_{6.5}C_{13.5}$ (This work)	RhB	100	0.3	1	3	0.21	0.37
$Fe_{80}P_{4.5}C_{15.5}$ (This work)	RhB	100	0.3	1	3	0.24	0.36
$Fe_{80}P_{13}C_7$ [19]	RhB	50	0.5	1	3	0.41	0.63
$Fe_{73.5}Si_{13.5}B_9Cu_1Nb_3$[49]	MB	20	0.5	1	3	0.119	0.111
$Fe_{78}Si_9B_{13}$ [49]	MB	20	0.5	1	3	0.302	0.258
$Fe_{81}Si_2B_{10}P_6Cu_1$[50]	MB	100	0.5	1	3	0.58	0.48
$Fe_{81}B_{10}C_9$[51]	MB	20	0.5	0.2	3.5	0.13	0.16
$(Fe_{73.5}Si_{13.5}B_9Cu_1Nb_3)_{91.5}Ni_{8.5}$[17]	MO	25	10	-	6	0.034	0.103
$Fe_{75}P_5C_{10}$[20]	RR195	100	0.5	1	3	0.221	0.349
$Fe_{77.2}Mo_{0.8}Si_9B_{13}$[52]	AO II	100	-	-	6	0.282	0.178
$Fe_{82}Si_{2.5}B_{12}P_{2.5}C$[18]	O II	-	2	-	-	0.06981	0.07806
$Fe_{78}Si_9B_{13}$[22]	3,5-DiClSA	-	4	4	7	0.0166	0.004

RhB Rhodamine B, *MB* Methylene Blue, *MO* Methyl Orange, *RR195* Reactive Red 195, *AO II* Acid Orange II, *O II* Orange II, *3,5-DiClSA* 3,5-Dichlorosalicylic Acid.

Table 6 | Current development of wastewater treatment using as spun and ball-milling ribbons under different conditions

Catalysts	Organic pollutants	c_{Dye} (mg·L^{-1})	$c_{catalysts}$ (g·L^{-1})	c_{H2O2} (mM)	pH	Reaction rate constant of as spun ribbon k_{AS} (min^{-1})	Reaction rate constant of after-processing ribbon k_{AP} (min^{-1})
$Fe_{80}Si_1P_{10}C_9$[10]	MB	120	0.5	1	3	0.4043	0.5333
$Fe_{70}Si_{10}B_{20}$[11]	MO	20	4	-	-	0.099	0.1
$Fe_{81}B_{13.5}Si_{3.5}C_2$[53]	MO	30	0.024	0.98	3	0.0548	0.0612
$Fe_{73.5}Si_{15.5}B_7Nb_3Cu_1$[13]	AO7	20	10	-	3	0.015	0.021

MB Methylene Blue, *MO* Methyl Orange, *AO7* Acid Orange 7.

Table 7 | Current development of wastewater treatment using as spun and dealloying ribbons under different conditions

Catalysts	Organic pollutants	Peroxide	c_{Dye} (mg·L^{-1})	$c_{catalysts}$ (g·L^{-1})	$c_{peroxide}$ (mM)	pH	Reaction rate constant of as spun ribbon k_{AS} (min^{-1})	Reaction rate constant of after-processing ribbon k_{AP} (min^{-1})
$Fe_{73.5}Si_{13.5}B_9Cu_1Nb_3$[14]	MB	PMS	20	0.5	1	3.4	0.021	0.064
$Fe_{50}Ni_{30}P_{13}C_7$[12]	BB-BN	H_2O_2	20	0.5	1	3	0.175	0.339

MB Methylene Blue, *PMS* Peroxymonosulfate, *BB-BN* Brilliant Black BN.

c_P = 4.5 and 6.5 at.% increase with increasing T_{an}, which shows a near-linear relationship between the k and ln (B_s·H_c).

In this work, the $Fe_{80}P_xC_{20-x}$ ingots and amorphous ribbons ($4.5 \le x \le 6.5$) have been arc melted and melt spun respectively. We have studied the microstructure, composition, Rhodamine B (RhB) degradation performance and magnetization performance of as spun and annealed ribbons with various methods. The following can be found:

(1) In present alloys, increasing P content (c_P) can inhibit the precipitation of primary α-Fe and graphite phases, and promote the formation of eutectic α-Fe + Fe_3C + Fe_3P phases in ingots and annealed ribbons. With increasing annealing temperature (T_{an}), the degradation performance and reusability of the ribbons with c_P = 4.5 at.% get better gradually and these of the ribbons with c_P = 6.5 at.% become better firstly and then worse; meanwhile, the saturation magnetisation (B_s) and coercivity (H_c) of the ribbons with c_P = 4.5 and 6.5 at.% increase with increasing T_{an}, which shows a near-linear relationship between the reaction rate constant k and ln (B_s·H_c).

(2) With increasing T_{an}, the primary α-Fe grain size of the ribbons with c_P = 4.5 at.% increases and their C atom segregation degree rises gradually; meanwhile, the α-Fe grain size of the ribbons with c_P = 6.5 at.% increases firstly and then decreases, due to the formation of eutectic α-Fe + Fe_3C + Fe_3P phases at high T_{an}. The T_{an}-dependent similarity between the α-Fe size and the degradation performance/reusability of measured ribbons can be explained by the size effect of galvanic cells in the ribbons' amorphous matrix and α-Fe precipitation: the larger the α-Fe size, the stronger the electron transportation.

(3) The ribbon with c_P = 6.5 at.% annealed at low T_{an} have the best degradation performance and reusability among 6 ribbons, and its P peak area increment (ΔA_{sum}) in XPS spectra after degradation is highest among 3 measured ribbons, which ascribes to the P element's role in accelerating Fe^{3+}/Fe^{2+} cycle. This work not only studies the mechanism of improving degradation performance for FePC amorphous alloys by annealing treatment, but also reveals a correlation between degradation performance and magnetization performance of FePC alloys.

Methods

Sample preparation

The $Fe_{80}P_xC_{20-x}$ (x = 4.5, 5, 5.5, 6 and 6.5) ingots were prepared by induction melting of pure raw materials of Fe (99.99 wt.%), pre-alloyed Fe-P ingots

(consisting of 71.5 wt.% Fe and 28.5 at.% P) and Fe-C ingots (consisting of 80 at.% Fe and 20 at.% C) in the arc melting furnace (MAM-1 Edmund Buhler) under the purified argon (99.999%). The pure raw materials were obtained from Beijing Jiaming Platinum Nonferrous Metals.

Then the obtained $Fe_{80}P_xC_{20-x}$ ($x = 4.5$, 5.5 and 6.5) ingots were remelted in quartz tube and spun into amorphous ribbons by single roller melt-spinning system (SD500 SKY) in the purified argon atmosphere. The roller speed was controlled at 46 m·s^{-1}. The ribbons with $x = 4.5$ and 6.5 were vacuum-annealed at 673 K, 717 K and 631 K, 671 K, 681 K, 727 K in the tube furnace (OTF-1200X-S-50) respectively. The heating rate of the annealing process was 10 K·min^{-1} and holding time was 20 min.

Microstructure characterization

The microstructure of the ingots and ribbons was examined by X-ray diffraction (XRD, Bruker D8 Discover) with Cu-Kα radiation. The microstructure of the ribbons was examined with a high resolution transmission electron microscope (TEM, FEI Talos F200). The thermal behavior of as spun ribbons was measured by differential scanning calorimetry (DSC, NETZSCH-404) under a flow of high purity argon with a heating rate of 20 K·min^{-1}. The surface morphology of the ingots and ribbons, and the fracture surface morphology of the ribbons were observed using a scanning electron microscope (SEM, JSM-7800F) equipped with an energy dispersive X-ray spectrometer (EDS). The ingots were corroded with 10% alcohol nitrate for 10 seconds before the surface morphology was observed. The binding energy of elements on the surface of the ribbons was evaluated by X-ray photoelectron spectroscopy (XPS, AXIS Supra) with a monochromatic Al Kα X-ray source ($h\nu = 1486.6$ eV).

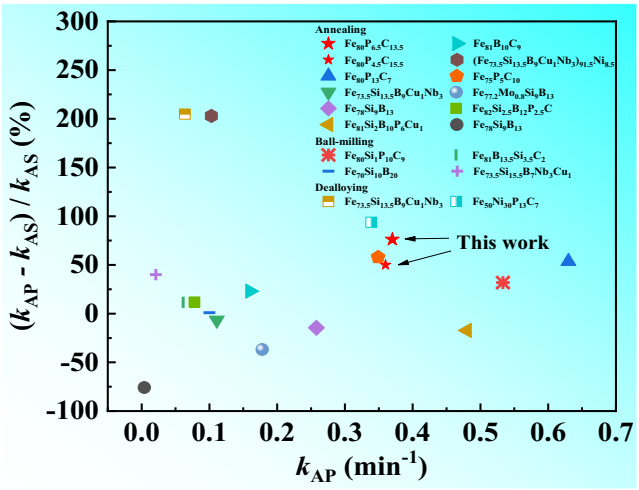

Fig. 12 | Degradation performance comparison of annealed $Fe_{80}P_{4.5}C_{15.5}$ ribbon ($P4_{an2}$), annealed $Fe_{80}P_{6.5}C_{13.5}$ ribbon ($P6_{an1}$) and the referenced materials, which be processed by corresponding amorphous alloys with different processing methods, including annealing, ball-milling and dealloying. k_{AS}: the reaction rate constant k of as spun ribbon; k_{AP}: the reaction rate constant k of the after-processing ribbon.

Physical tests

The mechanical properties of the ribbons were tested by nano-indentation test (HysitronTI980) and each ribbon was repeated three times. The contact angle (CA) of the ribbons was measured by optical contact angle measuring instrument (Theta Flex). The saturation magnetisation (B_s) of as spun and annealed ribbons and coercivity (H_c) of annealed ribbons were obtained by measuring the *B-H* hysteresis loops with a vibrating sample magnetometer (VSM, JDAW-2000D). The H_c of as spun ribbons was obtained by measuring the *B-H* hysteresis loops with a DC *B-H* loop tracer (Linkjoin MATS-2010SD). The magnetic permeability (μ) of the ribbons was measured by an inductance method permeability meter (Linkjoin MPT-1M).

Chemical tests

The ribbons were cut into 1 cm long stripes for degradation tests. RhB solution was prepared by commercially available synthetic dye Rhodamine B (RhB, $C_{28}H_{31}ClN_2O_3$, AR grade, Tianjin Beichen Fangzheng Reagent Factory, Tianjin, China, 100 mg·L^{-1}), Hydrogen peroxide (H_2O_2, AR grade, Tianjin Kemeo Chemical Reagent Co., Ltd. Tianjin, China, 1 mM) and Barnsted Nanopure water (18 MΩ cm). The pH of RhB solution was controlled by Hydrochloric acid (HCl, AR grade, Tianjin Hengxing Chemical Reagent Manufacturing Co., Ltd., Tianjin, China). 100 mL RhB solution ($T = 298$ K, pH = 3 and the ribbon dosage of 0.3 g·L^{-1}) was stirred at a fixed speed under the visible light if noted. The visible light was provided by the photocatalytic device combining the filter with the simulated sunlight xenon lamp light source (PL-X500) and the output current was controlled to 20 A. 3 mL of the solution was extracted by a syringe equipped with 22 μm membrane at selected time intervals and then tested by the UV-Vis spectrophotometer (UV-4802). In cyclic tests, the ribbons were extracted from

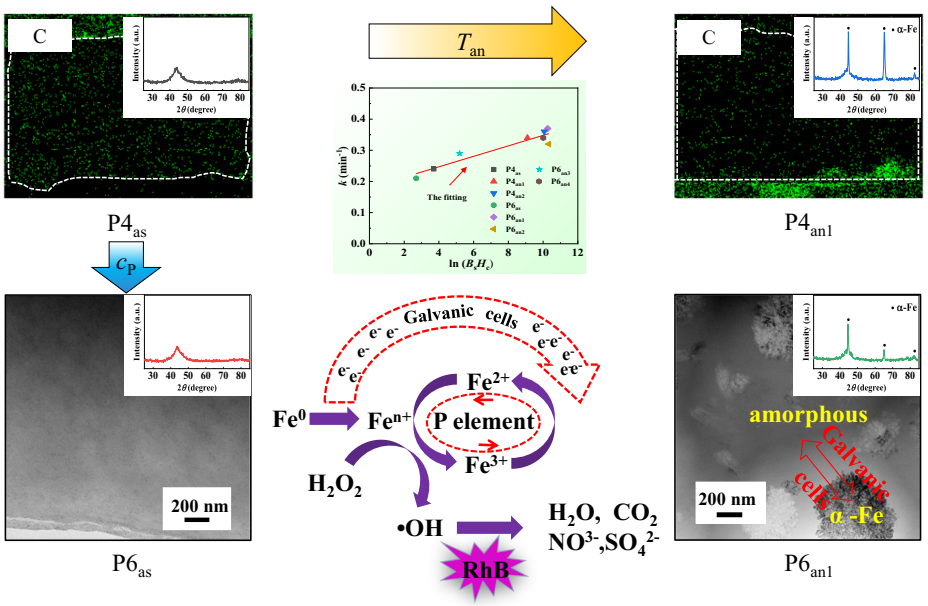

Fig. 13 | Schematic illustration of the pathway of RhB solution degradation for as spun and annealed $Fe_{80}P_xC_{20-x}$ ($x = 4.5$ and 6.5) ribbons ($P4_{as}$, $P4_{an1}$, $P6_{as}$ and $P6_{an1}$). Includes the element mapping and XRD analysis of $P4_{as}$ and $P4_{an1}$, the LRTEM images and XRD analysis of $P6_{as}$ and $P6_{an1}$, the reaction rate constant k vs. ln (B_s·H_c) of all the ribbons and the pathway of RhB solution degradation for the ribbons.

the solution after each degradation test and stir washed with deionized water for 30 s before putting them into the next reaction batch.

The electrochemical impedance spectra (EIS) test was carried out in a three-electrode cell with an electrochemical workstation (CHI 660E) and performed for the as spun and annealed ribbons with $c_P = 6.5$ at.% in RhB solution. The working electrodes were ribbons and the free surface was covered with epoxy resin. The reference electrode was a saturated calomel electrode (SCE) and the counter electrode was a platinum plate. Before the EIS test, the ribbons were pretreated at open circuit potential 1200 s until the potential fluctuation was less than 5 mV within 10 min. The frequency was set from 100 kHz to 0.01 Hz and the amplitude was ±10 mV. The relevant parameters were obtained by the mathematical and circuit model.

Data availability

The authors declare that all data supporting the findings of this study are available within the paper and its supplementary information files.

Received: 27 November 2023; Accepted: 8 March 2024;
Published online: 16 March 2024

References

1. Tang, Y., Shao, Y., Chen, N. & Yao, K. F. Rapid decomposition of direct blue 6 in neutral solution by Fe-B amorphous alloys. *Rsc Adv.* **5**, 6215–6221 (2014).
2. Robinson, T., McMullan, G., Marchant, R. & Nigam, P. Remediation of dyes in textile effluent: a critical review on current treatment technologies with a proposed alternative. *Bioresource Technol.* **77**, 247–255 (2001).
3. Núñez, J. et al. Application of electrocoagulation for the efficient pollutants removal to reuse the treated wastewater in the dyeing process of the textile industry. *J. Hazard. Mater.* **371**, 705–711 (2019).
4. Zhang, L. C., Jia, Z., Lyu, F., Liang, S. X. & Lu, J. A review of catalytic performance of metallic glasses in wastewater treatment: Recent progress and prospects. *Prog. Mater. Sci.* **105**, 100576 (2019).
5. Qi, Z. G. et al. Light activated methylene blue degradation by magnetic $Fe_{80}P_xC_{20-x}$ (x = 0, 4, 7 and 13) glassy ribbons. *J. Alloy. Compd.* **953**, 170135 (2023).
6. Li, H. G. et al. Efficient degradation capability of the FePCB amorphous alloy in acid orange 7 dye solution. *J. Mater. Res. Technol.* **26**, 6842–6856 (2023).
7. Si, J. J. et al. Porous composite architecture bestows Fe-based glassy alloy with high and ultra-durable degradation activity in decomposing azo dye. *J. Hazard. Mater.* **388**, 122043 (2020).
8. Jia, C. G. et al. Tailoring the corrosion behavior of Fe-based metallic glasses through inducing Nb-triggered netlike structure. *Corros. Sci.* **147**, 94–107 (2019).
9. Chen, Q. et al. Highly efficient catalytic performance and self-renewing behavior of Fe-based glass induced by pulsed laser. *J. Mater. Sci. Technol.* **188**, 191–201 (2024).
10. Ma, Y. Y. et al. Influence of surface morphology of Fe-based amorphous alloys on degradation of azo dye. *J. Phys. Chem. Solids.* **163**, 110596 (2022).
11. Xie, S. H., Peng, G. Q., Tu, X. M., Qian, H. X. & Zeng, X. R. Fe-based powders prepared by ball-milling with considerable degradation efficiency to methyl orange compared with Fe-based metallic glasses. *Acta Metall. Sin. (Engl. Lett.).* **31**, 1207–1214 (2018).
12. Liang, S. X. et al. Surface reactivation of FeNiPC metallic glass: A strategy for highly enhanced catalytic behavior. *J. Phys. Chem. Solids.* **132**, 89–98 (2019).
13. Miao, F. et al. Enhanced dye degradation capability and reusability of Fe-based amorphous ribbons by surface activation. *J. Mater. Sci. Technol.* **53**, 163–173 (2020).
14. Wang, J. C. et al. Chemically dealloyed Fe-based metallic glass with void channels-like architecture for highly enhanced peroxymonosulfate activation in catalysis. *J. Alloy. Compd.* **785**, 642–650 (2019).
15. Wang, J. Q. et al. Rapid degradation of azo dye by Fe-based metallic glass powder. *Adv. Funct. Mater.* **22**, 2567–2570 (2012).
16. Xie, S. H., Huang, P., Kruzic, J. J., Zeng, X. R. & Qian, H. X. A highly efficient degradation mechanism of methyl orange using Fe-based metallic glass powders. *Sci. Rep.-UK.* **6**, 21947 (2016).
17. Chen, S. Q. et al. Multi-phase nanocrystallization induced fast degradation of methyl orange by annealing Fe-based amorphous ribbons. *Intermetallics.* **90**, 30–35 (2017).
18. Chen, J. W. et al. Improving the degradation efficiency for the azo dye of $Fe_{82}Si_{2.5}B_{12}P_{2.5}C$ alloy via heat treatment. *Mater. Lett.* **300**, 130187 (2021).
19. Wang, Q. Q. et al. Effects of structural relaxation on the dye degradation ability of FePC amorphous alloys. *J. Non-Cryst. Solids.* **525**, 119671 (2019).
20. Chen, Q. et al. Nanostructured metallic glass contributing to efficient catalytic degradation of dye wastewater. *J. Non-Cryst. Solids.* **598**, 121952 (2022).
21. Chen, S. Q. et al. Unexpected high performance of Fe-based nanocrystallized ribbons for azo dye decomposition. *J. Mater. Chem. A.* **5**, 14230–14240 (2017).
22. Zhang, L. B. et al. Insight into efficient degradation of 3,5-dichlorosalicylic acid by Fe-Si-B amorphous ribbon under neutral condition. *Appl. Catal. B.* **294**, 120258 (2021).
23. Jia, Z. et al. Disordered atomic packing structure of metallic glass: toward ultrafast hydroxyl radicals production rate and strong electron transfer ability in catalytic performance. *Adv. Funct. Mater.* **27**, 1702258 (2017).
24. Hou, L., Shang, Q. Z., Yang, H., Zhang, B. & Huang, Y. Effects of oxygen on thermal behavior and magnetization performance of FePC. *amorphous alloy. J. Non-Cryst. Solids.* **581**, 121413 (2022).
25. Hou, L. et al. Structural responses of heterogeneous FeB(P)CCu amorphous alloys under nanoindentation. *J. Mater. Res. Technol.* **27**, 4109–4115 (2023).
26. Herzer, G. Modern soft magnets: Amorphous and nanocrystalline materials. *Acta Mater.* **61**, 718–734 (2013).
27. Han, M. H. et al. Revealing the effect of rapid annealing on nano-crystallization behavior and soft magnetization performance of Fe-Co-B amorphous alloy. *J. Mater. Res. Technol.* **26**, 5425–5436 (2023).
28. Azuma, D., Ito, N. & Ohta, M. Recent progress in Fe-based amorphous and nanocrystalline soft magnetic materials. *J. Magn. Magn. Mater.* **501**, 166373 (2020).
29. Ge, Y. X. et al. Remarkably enhanced Fenton-like catalytic activity and recyclability of Fe-based metallic glass by alternating magnetic field: mechanisms and industrial applications. *J. Mater. Chem. A.* **10**, 23314–23322 (2022).
30. Cai, L. et al. Key role of lorentz excitation in the electromagnetic-enhanced hydrogen evolution reaction. *ACS Appl. Mater. Inter.* **14**, 15243–15249 (2022).
31. Luo, J. et al. Low friction coefficient of superhard nc-TiC/a-C:H nanocomposite coatings deposited by filtered cathodic vacuum arc. *Mater. Res. Express.* **6**, 96418 (2019).
32. Meng, L. L. et al. Casting atmosphere effects on the precipitates, magnetism, and corrosion resistance of $Fe_{78}Si_9B_{13}$ glassy alloys. *Metall. Mater. Trans. A.* **44**, 5122–5133 (2013).
33. Wang, Q. Q. et al. Investigation of FePC amorphous alloys with self-renewing behaviour for highly efficient decolorization of methylene blue. *J. Mater. Chem. A.* **6**, 10686–10699 (2018).
34. Wang, X. F., Pan, Y., Zhu, Z. R. & Wu, J. L. Efficient degradation of rhodamine B using Fe-based metallic glass catalyst by Fenton-like process. *Chemosphere.* **117**, 638–643 (2014).
35. Zhang, L. C. & Liang, S. X. Fe-based metallic glasses in functional catalytic applications. *Chem. - Asian J.* **13**, 3575–3592 (2018).

36. Liu, Y. H. et al. Super plastic bulk metallic glasses at room temperature. *Science.* **315**, 1385–1388 (2007).
37. Zhang, X. Y. et al. Enhancement of nitrogen removal in hybrid wastewater treatment system using ferric citrate modified basalt fiber biocarrier. *Environ. Sci. Pollut. R.* **28**, 33480–33490 (2021).
38. Zhang, Y., Sharma, P. & Makino, A. Fe-Rich Fe-Si-B-P-Cu powder cores for high-frequency power electronic applications. *IEEE T. Magn.* **50**, 1–4 (2014).
39. Shi, M. J., Liu, Z. Q. & Zhang, T. Effects of metalloid B addition on the glass formation, magnetic and mechanical properties of FePCB bulk metallic glasses. *J. Mater. Sci. Technol.* **31**, 493–497 (2015).
40. Bitoh, T., Makino, A. & Inoue, A. Quasi-dislocation dipole-type defects and low coercivity of Fe-based soft magnetic glassy alloys. *J. Metastable Nanocryst. Mater.* **24-25**, 427–430 (2005).
41. Zhou, T. et al. Rapid decomposition of diclofenac in a magnetic field enhanced zero-valent iron/EDTA Fenton-like system. *Chemosphere.* **193**, 968–977 (2018).
42. Zha, L. et al. Growth of quasi-texture in nanostructured magnets with ultra-high coercivity. *Acta Mater.* **195**, 282–291 (2020).
43. Qi, Z. G. et al. Vacuum processing pressure and degradation performance of FePC ribbons in methylene blue solution. *J. Non-Cryst. Solids.* **576**, 121275 (2022).
44. Qin, C. L. et al. Novel bioactive Fe-based metallic glasses with excellent apatite-forming ability. *Mater. Sci. Eng. C.* **69**, 513–521 (2016).
45. Yao, Y. D. et al. Iron phosphide encapsulated in P-doped graphitic carbon as efficient and stable electrocatalyst for hydrogen and oxygen evolution reactions. *Nanoscale.* **10**, 21327–21334 (2018).
46. Zhou, H. Y. et al. Metal-free black-red phosphorus as an efficient heterogeneous reductant to boost Fe^{3+}/Fe^{2+} cycle for peroxymonosulfate activation. *Water Res.* **188**, 116529 (2021).
47. Chen, Q. et al. Insight into fast catalytic degradation of neutral reactive red 195 solution by FePC glassy alloy: Fe release and OH generation. *J. Mol. Liq.* **364**, 120058 (2022).
48. Rueda, F. et al. Characterization of venezuelan laterites by X-ray photoelectron spectroscopy. *J. Electron Spectrosc.* **82**, 135–143 (1996).
49. Liang, S. X. et al. Compelling rejuvenated catalytic performance in metallic glasses. *Adv. Mater.* **30**, 1802764 (2018).
50. Wang, Q. Q. et al. Competitive effects of structural heterogeneity and surface chemical states on catalytic efficiency of FeSiBPCu amorphous and nanocrystalline alloys. *ACS Appl. Nano Mater.* **2**, 214–227 (2019).
51. Wei, B. B., Li, X. L., Sun, H. G., Song, K. K. & Wang, L. Improved degradation capability of $Fe_{81}B_{10}C_9$ amorphous ribbon with the nanoscale layer rich of small atoms (B, C). *J. Non-Cryst. Solids.* **564**, 120838 (2021).
52. Zhang, C. Q. & Sun, Q. L. Annealing-induced different decolorization performances of Fe-Mo-Si-B amorphous alloys. *J. Non-Cryst. Solids.* **470**, 93–98 (2017).
53. Cherkezova-Zheleva, Z. et al. Application of mechanochemically treated waste materials for water remediation. *Phys. Status Solidi (A).* **219**, 2100515 (2022).

Acknowledgements

This work was financially supported by the Key Research and Development Program of China (Grant No. 2022YFB2404102), the National Natural Science Foundation of China (51971093, 52171158, and 52101196), the Open Project Program of Shandong Marine Aerospace Equipment Technological Innovation Center (Ludong University) (Grant No. MAETIC2021-11), and the Key R&D Program of Shandong Province, China (Grant No. 2021ZLGX01, 2022CXGC020308, 2023CXGC010308).

Author contributions

Conceptualization, Qi Z.G. and Chen Q.; Methodology, Wang Z.X., Song Z.Q. and Kim K.B.; Investigation, Qi Z. G., Wang Z.X. and Pang J.; Data Curation, Qi Z.G. and Chen Q.; Writing-Original Draft Preparation, Qi Z.G.; Writing-Review and Editing, Qi Z.G., Wang W.M. and Pang J.; Supervision, Wang W. M. and Zhang X.H.

Competing interests

The authors declare no competing interests.

Additional information

Supplementary information The online version contains supplementary material available at https://doi.org/10.1038/s41529-024-00449-7.

Correspondence and requests for materials should be addressed to X. H. Zhang or W. M. Wang.